PHYSICAL DEVICES FOR ECOLOGY,
MEDICINE, BIOLOGY

EXPERIMENTAL STUDY OF A GRID SENSOR FOR MEASURING THE VELOCITY VECTOR OF MICROMETEOROIDS AND SPACE DEBRIS PARTICLES

© 2025 M. P. Kalaev, A. M. Telegin*, K. E. Voronov

Samara National Research University

named after academician S.P. Korolev Russia, Samara

**e-mail:talex85@mail.ru*

Received April 19, 2024

Revised June 24, 2024

Accepted July 08, 2024

Abstract. A description of a prototype sensor for measuring the velocity vector of micrometeoroids and space debris particles based on grid metal electrodes is given. The results of an experimental study and proposals for further modification of the measurement system are presented.

DOI: 10.31857/S00328162250109e2

1. INTRODUCTION

Microparticles (space debris and micrometeoroids) in space are charged to a certain electric potential [1, 2]. To measure the speed**V**= {Vx, Vy, Vz} of these microparticles, the phenomenon of current induction by a charged moving body during its flight through measuring metals is mainly usedelectrodes (grids) [2–8]. The velocity vector of these microparticles can be used to estimate their kinetic energy, as well as the direction of arrival at the sensor, which allows predicting the source of their origin [9–11]. In addition to induction methods for measuring the velocity vector, there are also optical measurement methods, but, unfortunately, from the point of view of design implementation, they have a number of disadvantages, such as parasitic illumination, the impossibility of determining the charge of microparticles, etc. [12–14].

2. DESCRIPTION OF THE GRID SENSOR MEASUREMENT PRINCIPLE

Figure 1 shows a block diagram of a velocity vector meter, where positions *1 – 6* indicate measuring metal grids connected to two different amplifiers. A high-speed charged microparticle, flying through these grids along trajectory *7,* induces a current pulse on each grid, the shape of which is close to bell-shaped and whose parameters are proportional to the velocity and charge of this microparticle [9, 11]. The peak of signals from the grids corresponds to the moment when the particle passes through the

grid, which allows fixing the moment of passage. Grids *1* and *6* are located in planes parallel to the *XOY* plane. Grids *2* and *3* are parallel to each other, positioned at a certain angle *A* to the *XOY* plane and perpendicular to the *XOZ* plane. Grids *4* and *5* are parallel to each other, positioned at a certain angle *B* to the *XOZ* plane and perpendicular to the *XOY* plane [9]. In the considered design, angles *A* and *B* are equal to 15°.

Fig. 1. Block diagram of the microparticle velocity vector measurement sensor: *1 – 6* – grid electrodes; *7* – microparticle trajectory; *8* , *9* – amplifiers.

Let us denote by n the grid number, t_n – the time when the charged particle passes through the n-th grid, x_n, y_n, z_n – the point where the charged particle passes through the *n* -th grid (marked with a bold dot in Fig. 1), z_{n1} – the point where the n-th grid intersects the *OZ* axis. Then the components of the microparticle velocity vector can be determined according to formulas

$$Vz = (z_6 - z_1)/(t_6 - t_1),$$

$$Vx = (x_3 - x_2)/(t_3 - t_2) = \mathrm{ctg(A)}\left(Vz(t_3 - t_2) + (z_{31} - z_{21})\right)/(t_3 - t_2),$$

$$Vy = (y_5 - y_6)/(t_5 - t_6) = \mathrm{ctg(B)}\left(Vz(t_5 - t_4) + (z_{51} - z_{41})\right)/(t_5 - t_4).$$

In most cases, it is not necessary to know all three coordinates of the velocity vector, but only the magnitude of the velocity vector and its inclination to the target plane, which is hit by the high-speed microparticle. Assuming that the target plane is parallel to the *XOY* plane, we get the following expressions:

$$V = \sqrt{Vx^2 + Vy^2 + Vz^2}$$

– the magnitude of the velocity vector,

$$\gamma = \arccos\left(\left(Vx^2 + Vy^2\right)/\sqrt{Vx^2 + Vy^2 + Vz^2}\right)$$

– the angle of inclination to the target plane.

3. EXPERIMENT DESCRIPTION

Figure 2 shows the placement of the developed prototype sensor in the vacuum chamber of the microparticle accelerator, the operating principle of which is described in detail in works [10, 15].

Fig. 2. Photos of the microparticle velocity vector sensor prototype installed in the accelerator vacuum chamber: **a** – rear view, **b** – side view.

The block diagram of the test bench for conducting experiments with the microparticle sensor is shown in Fig. 3.

Fig. 3. Block diagram of the test bench for calibrating the velocity vector sensor:

The base of the sensor prototype was manufactured using a 3D printer by FDM printing from ABS plastic. The dimensions of the model are 100×100×100 mm ^{3}, the dimensions of the sensitive window are 80×80 mm ^{2}. When manufacturing grid frames, two technologies were tested: 3D printing and milling of foil-clad fiberglass on a CNC machine. Using 3D printing allows for accelerating the prototyping process and obtaining frames with minimal parasitic capacitance; however, plastic is unsuitable for creating onboard equipment due to its low resistance to space factors. Nichrome wire with a thickness of 30 μm was used as the grid string material, with a distance between strings of 5 mm. Nichrome was chosen due to its high mechanical strength at small string thickness, despite its relatively high specific resistance [10]. Preliminary experiments have shown that the use of other conductors, such as copper, has practically no effect on the shape and amplitude of the induced signals.

As a result of the experiment, time intervals of the particle passing through six grids and two Faraday cups were recorded [15]. The change in the microparticle's entry angle into the sensor was accomplished by rotating the sensor itself relative to the accelerator path axis, which coincides with the axis of the Faraday cups. A 28-BYJ48 stepper motor with an integrated gearbox was used as the rotation device. The motor has 64 steps per revolution, which, together with the 1/63.68395 gear ratio, allows the output rotor to be rotated with a step of approximately 0.087°. Since such small rotation angles were not required during the initial tests of the sensor prototype, rotation was performed with a 6° step in the angle range from -42° to +42° (relative to the accelerator axis). The stepper motor operation was controlled by a microcontroller (MC) and a stepper motor driver (SMD) located outside the vacuum chamber, and commands to the microcontroller were sent from a computer through a galvanic isolation module (GI).

The circuit uses two amplifiers, A_1 and A_2, the electrical schematic of which is shown in Fig. 4 [16]. The Faraday ring K_1 is connected to grids G_1, G_3, G_5 and is connected to the input of amplifier A_1. The Faraday ring K_2 is connected to grids G_2, G_4, G_6 and is connected to the input of amplifier A_2. This connection scheme allows reducing the number of analog recording channels from eight to two, which simplifies recording and subsequent signal processing during sensor prototype testing. When a particle passes through any of the grids, the adjacent grids function as shielding grids, as they are connected to the input of another amplifier configured with a "virtual ground" at the input. This

approach allows increasing the steepness of transit pulses without using an additional group of separating grounded grids, which increases the "transparency" coefficient of the sensor, which for this prototype is 97%. Tin powder with particle sizes of 1-2 μm was used as particles. With a voltage of 100 kV on the linear part of the accelerator, particle velocities were 100-900 m/s. In the course of further experiments, after optimizing the sensor design and amplifier circuit, tests at higher speeds are planned.

Fig. 4. Schematic diagram of the charge-sensitive amplifier.

Each of the amplifiers consists of three stages (Fig. 4). The conversion of charge to voltage is carried out using the first stage, implemented on the OPA656 chip (DA_1). The voltage at the output of the first stage is determined by the expression

$$U=-Q/C_1,$$

where Q is the charge of the microparticle, C_1 =10 pF is the capacitance in the feedback circuit of the first operational amplifier.

The second cascade, built on the operational amplifier AD8005 (DA_2), is an inverting voltage amplifier with a gain of 39. Capacitor C_4 together with resistor R_2 form a high-pass filter with a cutoff frequency of about 100 Hz, which helps reduce interference from the 50 Hz electrical network in laboratory conditions.

The third cascade is a non-inverting amplifier built on the OPA820 chip (DA_3). This cascade is designed to ensure the operation of the amplifier connected to the oscilloscope on a long coaxial line.

A four-channel Rigol MSO5104 oscilloscope with a maximum sampling rate of 6 GSPS was used as the recording equipment. The oscilloscope is powered through a galvanic isolation unit in the 220 V power supply chain to prevent 50 Hz network frequency interference from penetrating through the amplifier cables into the vacuum chamber. During the experiment, the oscilloscope is in standby mode with recording triggered when a specified threshold level is exceeded. Recording was conducted simultaneously on two channels with a sampling rate of 1 GSPS and a recording depth of 10 million samples per channel. The recorded packet was transferred to the computer via Ethernet protocol for subsequent processing.

Figure 5 shows the results of recorded transit pulses from the Faraday cups (K_1, K_2) and grids S_1 - S_6.

Fig. 5. Examples of oscillograms of induced pulses:

Figures 6 and 7 show the measurement errors of the microparticle velocity magnitude and their entry angle into the sensor. During the experiment, the minimum measured charge was 10^{-14} C.

Fig. 6. Error in measuring the velocity magnitude depending on the microparticle entry angle δ_V .

Fig. 7. Error in measuring the angle depending on the microparticle entry angle δ_α .

4. CONCLUSION

As a result of the conducted research, the following conclusions can be drawn. The presented sensor prototype has a modular design, which allows for quick modifications of the grid arrangement and measurements of the velocity vector magnitude and the entry angle of microparticles. Connecting multiple grids to the input of a single amplifier inevitably worsens the signal-to-noise ratio of the system and reduces the operating speed due to increased input capacitance. In the future, we plan to optimize the sensor design, develop and manufacture a multi-channel data recording system (with separate recording channels for each grid), which can be placed in close proximity to the sensor (inside the vacuum chamber).

The results of the conducted research showed that at large entry angles of microparticles into the sensor, the number of microparticle losses increases due to their impact on the measuring grids. This can be avoided by increasing the transparency of the grids.

The error in the measurements is most likely related to the manufacturing and mounting tolerance of the grids (about 0.5 mm). The measurement error increases with the increase in the angle of incidence of the microparticle, which is most likely associated with the large error in measuring V_x and V_y, caused by the small distances between grids C_2 and C_3, C_4 and C_5 . Additionally, microparticle velocity measurements can be conducted by analyzing the shape of the induced pulse, since, according to Fig. 5a, b, the form of the induced pulse depends on the entry angle of the microparticle. Such a method will likely have a greater error than the method of measuring time readings, which is related to the inaccuracy in estimating pulse amplitudes and the influence of internal and external noise [8, 17]. On the other hand, the combination of these two methods in the future will allow for a reduction in the number of measuring grids, thus decreasing the mass and dimensions of the sensor, which is important for applications on spacecraft.

REFERENCES

1. *Mironov V.V., Tolkach M.A.* // Space Engineering and Technology. 2022. № 1(36). P.125. https://doi.org/10.33950/spacetech-2308-7625-2022-1-125-143.

2. *Auer S., Grün E., Kempf S., Srama R., Srowig A., Sternovsky Z., Tschernjawski V* // Rev. Sci. Inst. 2008. V. 79. Art.№084501. https://doi.org/10.1063/1.2960566.

3. *Xie J., Sternovsky Z., Auerd S., Drake K., Grün E., Horanyi M., Le H., Srama R* // Planetary and Space Science. 2013. V. 89. P. 63. https://doi.org/10.1016/j.pss.2013.01.004.

4. *Auer S.* // Optica Acta. 1982. V. 29. № 10. P. 1421. https://doi.org/10.1080/713820766

5. *Auer S* // Rev. Sci. Instrum. 1975. V. 46. № 2. P. 127. https://doi.org/10.1063/1.1134155.

6. *Horányi M.* // Annu. Rev. Astron. Astrophys. 1996. V. 34. P. 383. https://doi.org/10.1146/annurev.astro.34.1.383.

7. *Auer S., Grün E., Srama R., Kempf S., Auera R* // Planetary and Space Science. 2002. V. 50. P. 773. https://doi.org/10.1016/S0032-0633(02)00019-3.

8. *Li Y., Kempf S., Simolka J., Strack H., Grün E, Srama R.* // Advances in Space Research. 2017. V. 59. P. 1636. https://doi.org/10.1016/j.asr.2016.12.037

9. *Telegin A.M., Voronov K.E., Shestakov D.A* // Engineering Physics. 2024. № 1. P. 49. https://doi.org/10.25791/infizik.1.2024.1381.

10. *Voronov K.E., Piyakov I.V., Kalaev M.P., Telegin A.M.* // Instruments and Experimental Techniques. 2023. № 6. P. 135. https://doi.org/10.1134/S0020441223040176.

11. *Poklonsky N.A., Vyrko S.A., Kocherzhenko A.A* // Technical Physics. 2004. V. 74. № 11. P. 75.

12. *Kalaev M.P., Rodina A.V., Telegin A.M., Ismagilova E.V.* // Instruments and Experimental Techniques. 2023. № 6. P. 142. https://doi.org/10.1134/S0020441223060027.

13. *Wang W., Xue W., Wu S., Mu Z., Yi J., Tang A.J.* // Materials. 2022. V. 15. P. 3871. https://doi.org/10.3390/ma15113871.

14. *Weiner I., Rust M., Donnelly T.D.* // Am. J. Phys 2001. V. 69. P. 129. https://doi.org/10.1119/1.1311785

15. *Piyakov A.V., Telegin A.M.* // Instruments and Experimental Techniques. 2022. № 4. P. 106. https://doi.org/10.31857/S0032816222040243.

16. *Thomas E., Simolka J., DeLuca M., Horányi M., Janches D., Marshall R.A., Munsat T., Plane J.M.C., Sternovsky Z.* // Rev. Sci. Instrum. 2017. V. 88. P. 034501. https://doi.org/: 10.1063/1.4977832.

17. *Voronov K.E., Telegin A.M., Sukhachev K.I., Kalaev M.P.* // UPF. 2020. Vol. 8. No. 6. P. 411.

FIGURE CAPTIONS

Fig. 1. Block diagram of microparticle velocity vector sensor: *1* - *6* - grid electrodes; *7* - microparticle trajectory; *8* , *9* - amplifiers.

Fig. 2. Photos of the microparticle velocity vector sensor prototype installed in the accelerator vacuum chamber: **a** - rear view, **b** - side view.

Fig. 3. Block diagram of the velocity vector sensor calibration stand: C_1 - C_6 - metal grids; K_1 , K_2 - Faraday rings, A_1 , A_2 - amplifiers; PSA - power supply for amplifiers; *M* - stepper motor; *GI* - galvanic isolation of digital interface; *MC* - microcontroller; *SMD* - stepper motor driver; *OSC* - digital oscilloscope; *GIP* - galvanically isolated oscilloscope power supply.

Fig. 4. Circuit diagram of the charge-sensitive amplifier.

Fig. 5. Examples of induced pulse oscillograms: **a** - sensor axis is positioned at zero angle relative to accelerator beam axis; **b** - sensor axis is positioned at 25° angle relative to accelerator beam axis; **c** - oscillogram showing microparticle impact on grid C_1 .

Fig. 6. Velocity magnitude measurement error depending on microparticle incident angle δ_V .

Fig. 7. Angle measurement error depending on microparticle incident angle δ_α .

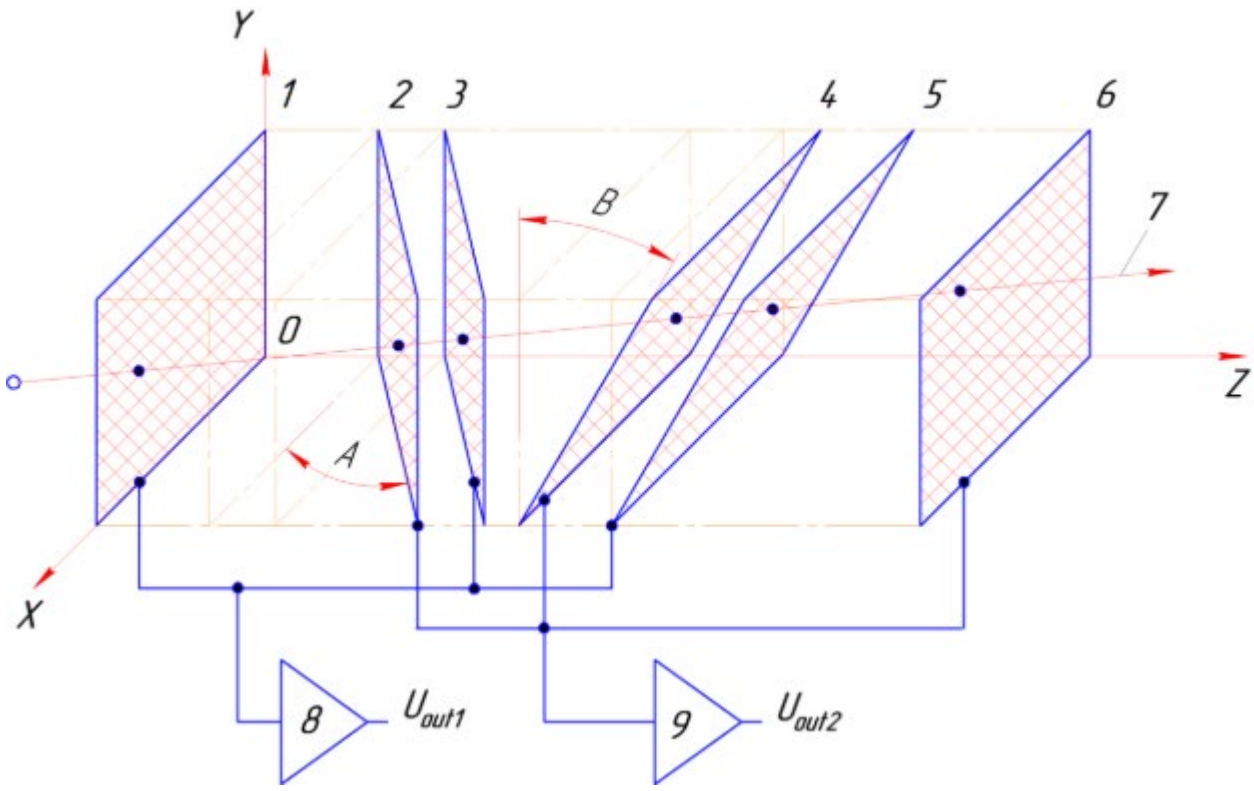

Fig. 1.

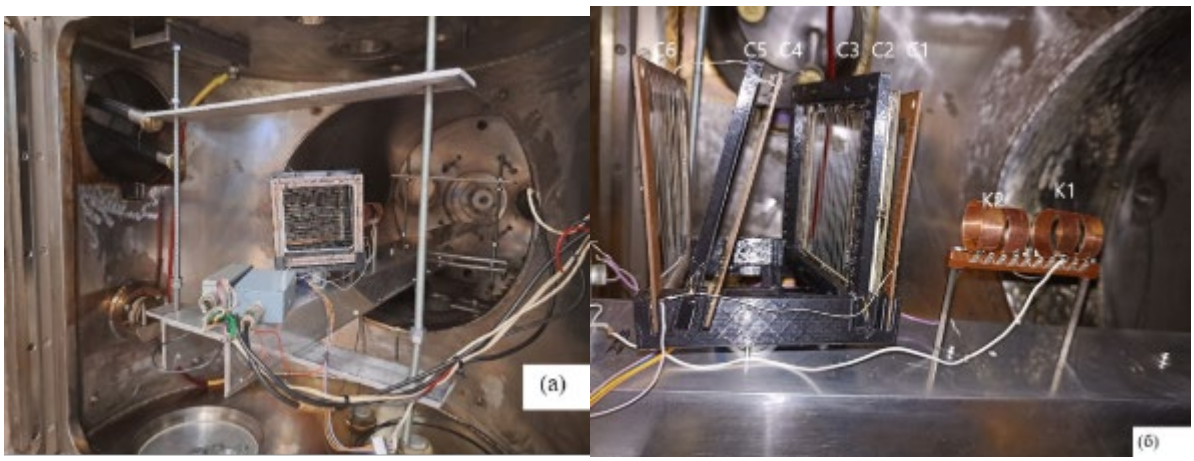

Fig. 2.

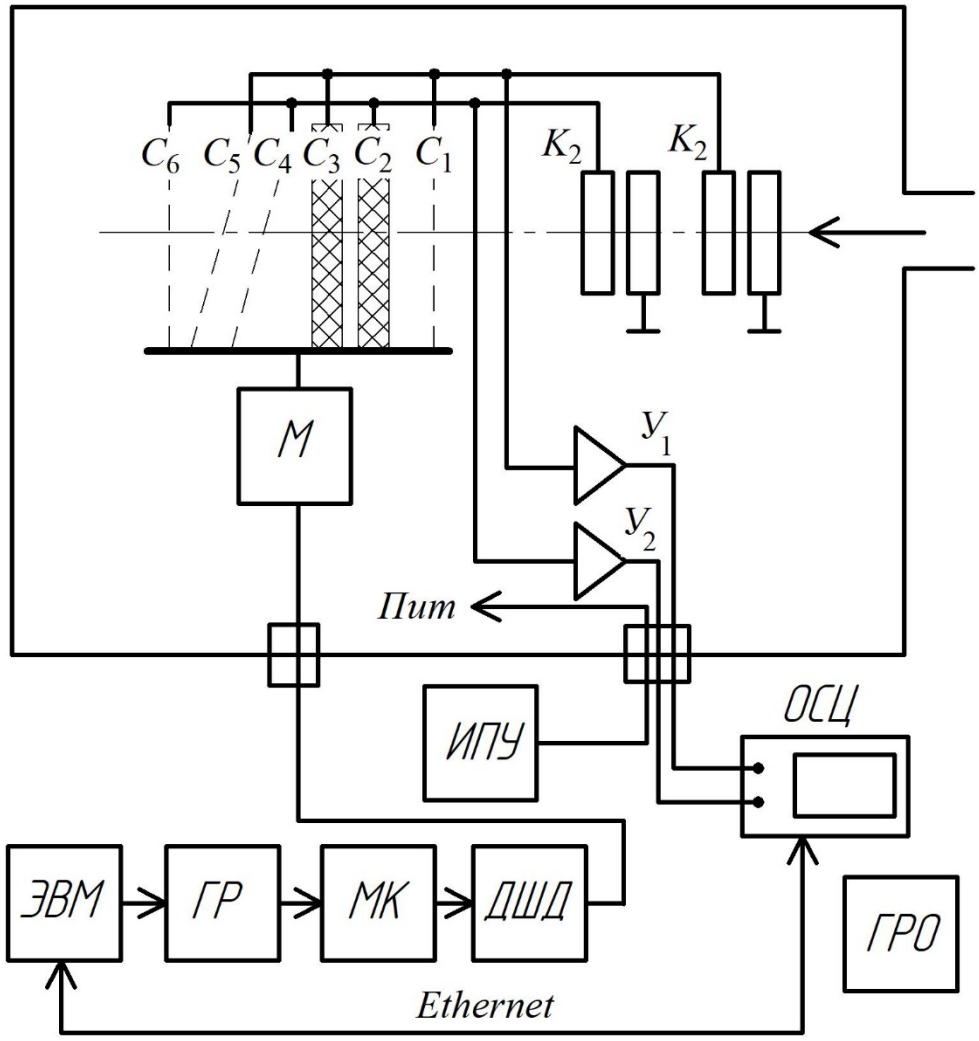
C6
C5
C4
C3
C2
C1
K2
K2
M
У1
У2
Пит
ИПУ
ОСЦ
ЭВМ
ГР
МК
ДШД
ГРО
Ethernet

Fig. 3.

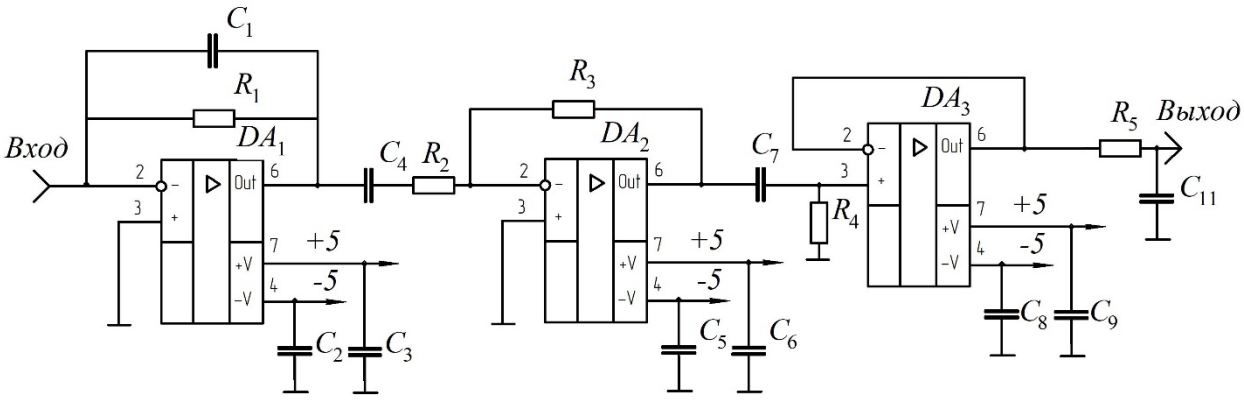
C1
R1
Вход
DA1
C4
R2
R3
DA2
C7
DA3
R5
Выход
C11
R4
+5
-5
C2
C3
C5
C6
C8
C9

Fig. 4.

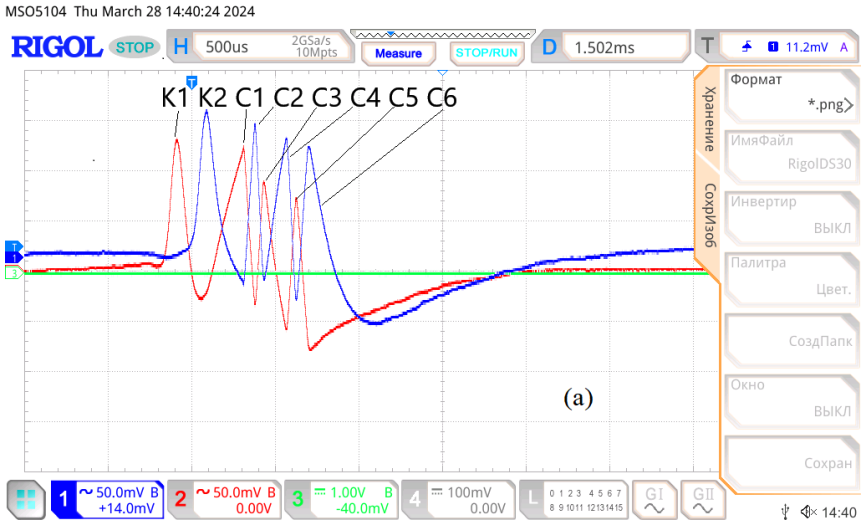
MSO5104 Thu March 28 14:40:24 2024
RIGOL
STOP
500us
Measure
STOP/RUN
1.502ms
11.2mV
K1 K2 C1 C2 C3 C4 C5 C6
(а)
Формат
*.png
ИмяФайл
RigolDS30
Инвертир
ВЫКЛ
Палитра
Цвет.
СоздПапк
Окно
ВЫКЛ
Сохран
Хранение
СохрИзоб
50.0mV
+14.0mV
50.0mV
0.00V
1.00V
-40.0mV
100mV
0.00V
14:40

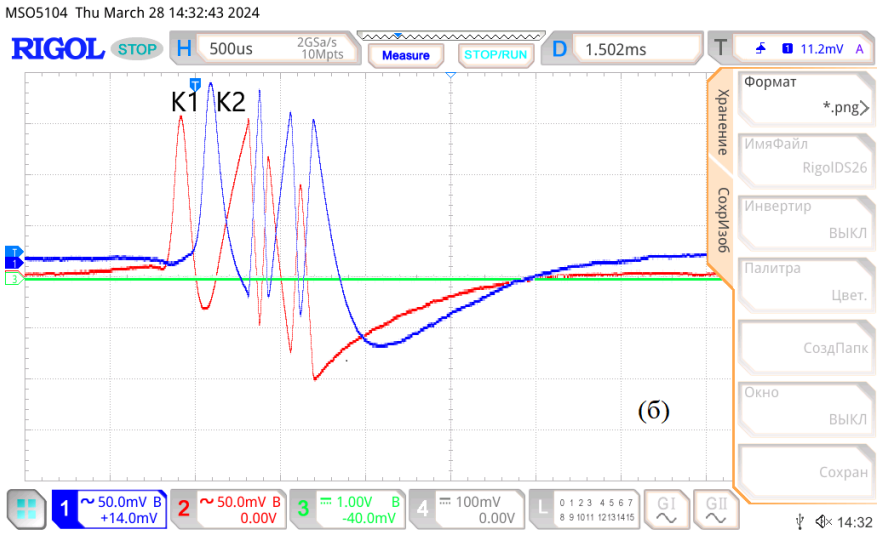
MSO5104 Thu March 28 14:32:43 2024
RIGOL
STOP
500us
Measure
STOP/RUN
1.502ms
11.2mV
K1 K2
(б)
Формат
*.png
ИмяФайл
RigolDS26
Инвертир
ВЫКЛ
Палитра
Цвет.
СоздПапк
Окно
ВЫКЛ
Сохран
Хранение
СохрИзоб
50.0mV
+14.0mV
50.0mV
0.00V
1.00V
-40.0mV
100mV
0.00V
14:32

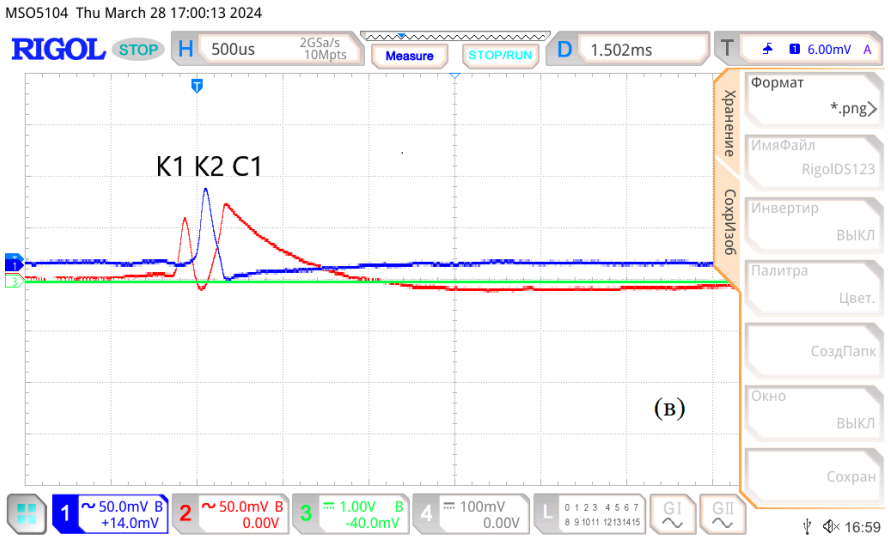
MSO5104 Thu March 28 17:00:13 2024
RIGOL
STOP
H 500us
2GSa/s
10Mpts
Measure
STOP/RUN
D 1.502ms
T
6.00mV A
K1 K2 C1
(в)
Формат
*.png
ИмяФайл
RigolDS123
Инвертир
ВЫКЛ
Палитра
Цвет.
СоздПапк
Окно
ВЫКЛ
Сохран
Хранение
СохрИзоб
1 50.0mV B
+14.0mV
2 50.0mV B
0.00V
3 1.00V B
-40.0mV
4 100mV
0.00V
16:59

Fig. 5.

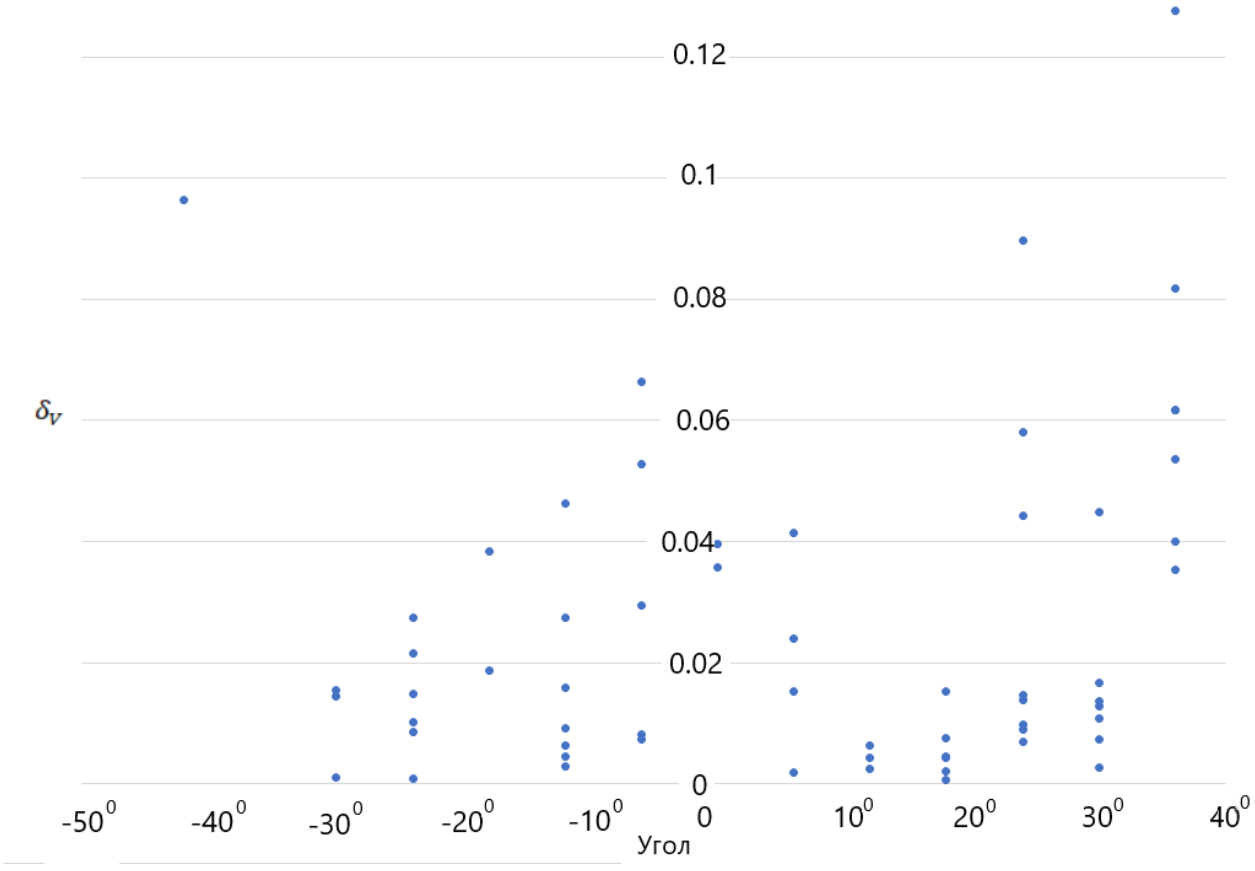
0.12
0.1
0.08
0.06
0.04
0.02
0
δ_V
-50⁰
-40⁰
-30⁰
-20⁰
-10⁰
0
10⁰
20⁰
30⁰
40⁰
Угол

Fig. 6.

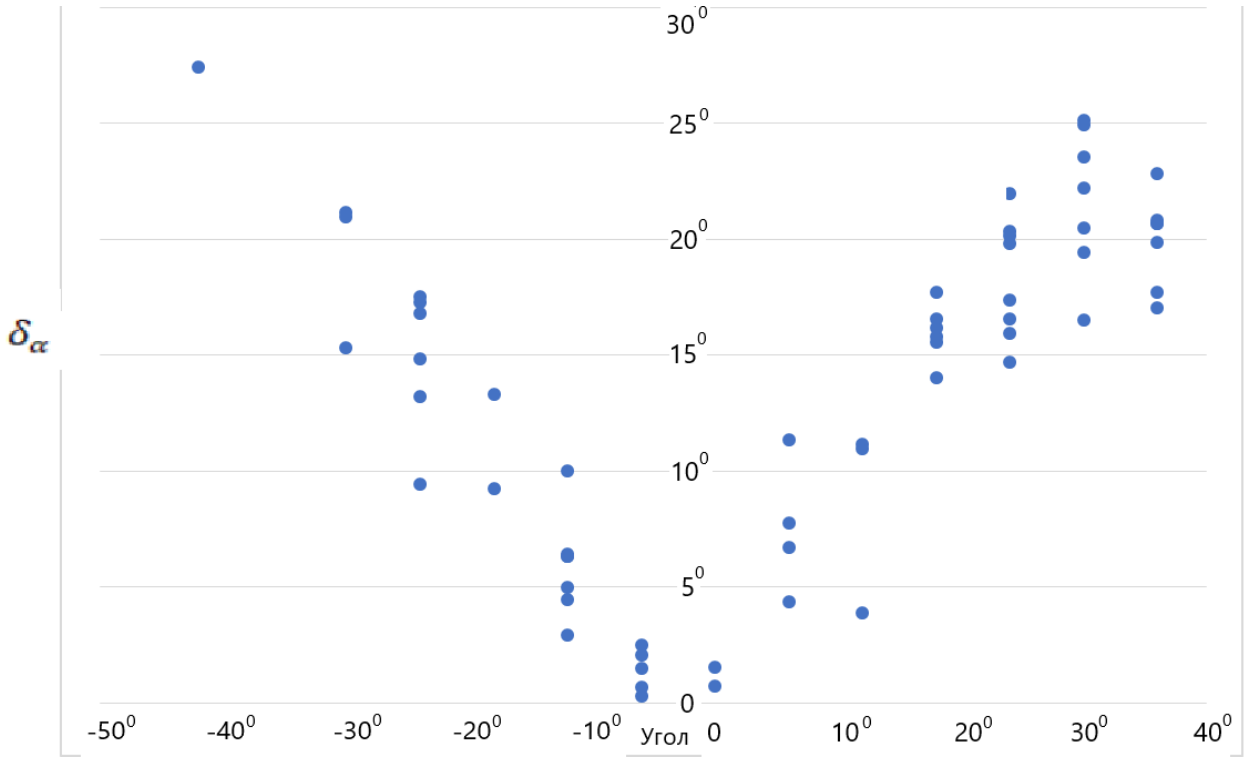
δ_α
30⁰
25⁰
20⁰
15⁰
10⁰
5⁰
0
-50⁰
-40⁰
-30⁰
-20⁰
-10⁰
Угол
0
10⁰
20⁰
30⁰
40⁰

Fig. 7.